**Atmospheric
Measurement
Techniques
Discussions**

Tomographic retrieval approach for mesoscale gravity wave observations by the PREMIER Infrared Limb-Sounder

J. Ungermann, L. Hoffmann, P. Preusse, M. Kaufmann, and M. Riese

Forschungszentrum Jülich, Institut für Chemie und Dynamik der Geosphäre (ICG-1),
Jülich, Germany

Correspondence to: J. Ungermann (j.ungermann@fz-juelich.de)

AMTD

2, 2809–2850, 2009

**Tomographic
retrieval approach for
gravity wave
observations**

J. Ungermann et al.

Title Page

Abstract	Introduction
Conclusions	References
Tables	Figures

| ◄◄ | ►► |
| ◄ | ► |

Back | Close

Full Screen / Esc

Printer-friendly Version

Interactive Discussion

Abstract

PREMIER is one of three candidates for ESA's 7th Earth Explorer mission that are currently undergoing feasibility studies. The main mission objective is to quantify processes controlling atmospheric composition in the mid/upper troposphere and lower stratosphere, a region of particular importance for climate change. To achieve this objective, PREMIER will employ the first satellite Fourier transform infrared limb-imager combined with a millimetre-wave limb-sounder. The infrared limb-imager can be operated in a high spatial resolution mode ("dynamics mode") for observations of small-scale structures in atmospheric temperatures and trace gas fields with unprecedented 3-D sampling (0.5 km in the vertical direction, 50 km along track, 25 km across track). In this paper, a fast tomographic retrieval scheme is presented, which is designed to fully exploit the high-resolution radiance observations of the dynamics mode. Based on a detailed analysis of the "observational filter", we show that the dynamics mode provides unique information on global distributions of gravity waves (GW). The achievable vertical resolution for GW observations has values between the vertical sampling (0.5 km) of the dynamics mode and the vertical field of view (about 0.75 km). The horizontal across track resolution corresponds to the horizontal across track sampling of 25 km. Since the achievable along track horizontal resolution is about 70 km, the dynamics mode will provide, for the first time, GW limb-observations with a horizontal resolution comparable to nadir sounders. Compared to previous observations, PREMIER will therefore considerably extend the range of detectable GWs in terms of horizontal and vertical wavelength.

1 Introduction

Numerous previous satellite missions have used the infrared limb-emission sounding technique for atmospheric remote sensing. Global observation of atmospheric infrared limb-emissions represents a reliable technique to obtain vertically resolved profile data

of temperature, a variety of trace gases, aerosols, and clouds simultaneously, at day-time and at night-time. First global infrared limb-emission observations of an extensive number of atmospheric trace species were made by LIMS (Limb Infrared Monitor of the Stratosphere; Gille and Russel III, 1984) and SAMS (Stratospheric and Mesospheric Sounder; Drummond et al., 1980) aboard the NIMBUS 7 satellite. Trace gas fields obtained from these sensors and follow-on instruments such as the CRISTA instrument (Riese et al., 1999) greatly contributed to our understanding of the three-dimensional composition, structure and large-scale dynamics of the middle atmosphere. Early 2002 EGA launched Envisat, a polar-orbiting Earth observation satellite, which included the Michelson Interferometer for Passive Atmospheric Sounding (MIPAS) instrument (Fischer et al., 2008) for infrared limb-emission observations with high spectral resolution. MIPAS significantly expanded the number of detectable species and the corresponding height range compared to previous space missions.

All previous instruments have used telescopes with scanning mirrors or one-dimensional detector arrays to obtain profile information of atmospheric trace species. While previous instruments were rather restricted in terms of spatial resolution (and in particular horizontal sampling), the PEMIER mission (ESA, 2008) employs an InfraRed Limb-Sounder (hereafter IRLS) that builds on recent developments in infrared detector array technology providing the basis for an instrument capable of achieving the high three-dimensional (3-D) spatial resolution, necessary to sense the upper troposphere/lower stratosphere (UTLS) region (Riese et al., 2005; Friedl-Vallon et al., 2006). During the PREMIER mission (Process Exploration through Measurements of Infrared and millimetre-wave Emitted Radiation) the IRLS can be operated in two different operating modes. The one discussed in this paper, the "dynamics mode", is designed for unprecedented 3-D spatial sampling and is thereby optimised to resolve small and mesoscale atmospheric temperature and trace gas structures (e.g. Adams et al., 2009). The sampling is 0.5 km in the vertical direction, 25 km across track (in a 320 km swath), and 50 km in the along track direction. The across track sampling corresponds to the achievable across track resolution. To fully exploit the benefits of

Tomographic retrieval approach for gravity wave observations

J. Ungermann et al.

the dense sampling in the vertical and along track direction in terms of resolution, we present a new tomographic retrieval scheme. Tomographic retrievals for limb sounding measurements were first explored by Carlotti et al. (2001) for MIPAS and Livesey and Read (2000) for MLS (Microwave Limb Sounder). By using a very fast and efficient

5 forward model (Hoffmann et al., 2008; Hoffmann and Alexander, 2009) we are able to explore the approach at smallest spatial scales that were not assessed by previous studies (e.g. Carlotti et al., 2006; Steck et al., 2005). In particular, our analysis demonstrates the capability of the PREMIER IRLS to provide unique global information on meso-scale gravity waves (GW).

10 Global observations of GWs is a major objective of the PREMIER mission (ESA, 2008). GWs represent an important coupling mechanism for the middle atmosphere (Fritts and Alexander, 2003). They contribute to the driving of the quasi-biennial oscillation by about 50% (Dunkerton, 1997), are the major forcing mechanism of the summer branch of the Brewer-Dobson circulation (Alexander and Rosenlof, 2003), and con-

15 tribute 30 to 50% to the predicted increase of the Brewer-Dobson circulation due to climate change (McLandress and Shepherd, 2009). GWs are also the main driver of mesospheric winds and cause the cold summer mesopause (McLandress, 1998). Currently, uncertainties in the global representation of GWs and their effects on the circulation represent a major limitation for the predictive capabilities of chemistry climate

20 models (CCM) at present time.

The great potential of GW observations from space has been demonstrated in several studies (e.g. Eckermann and Preusse, 1999; Preusse et al., 2002). However, the spatial resolution of previous global observations was insufficient for the determination of direction-resolved momentum flux (Ern et al., 2004). The combination of

25 high-resolution 3-D temperature measurements and good altitude coverage offered by PREMIER will allow for simultaneous determination of GW temperature amplitudes and associated horizontal and vertical wavelength (wave-vector). Preusse et al. (2009) showed that global 3-D observations by limb-imagers such as PREMIER provide the best perspective to obtain global information of GW momentum flux.

For the interpretation of the results, it is crucial to accurately determine the observational filter (Alexander, 1998) of the limb-imaging technique employed by the PREMIER IRLS. The observational filter describes the reproduction of GW amplitudes by the retrieval scheme as function of vertical and horizontal wavelength. A precise characterisation of the observational filter is also essential for comparisons with other measurement techniques (Preusse et al., 2000; Hertzog et al., 2008) as well as for comparisons with GW resolving models or results obtained from GW parameterisation schemes (Ern et al., 2004, 2005).

In Sect. 2, we briefly introduce the dynamics mode of the PREMIER IRLS. We present our simulation setup in Sect. 3 followed by the JURASSIC forward model in Sect. 4 and finally the tomographic retrieval approach in Sect. 5. The results regarding achievable resolution and GW observational filter are presented in Sect. 6.

2 The PREMIER Infrared Limb Sounder

The PREMIER IRLS essentially combines a Fourier transform infrared spectrometer with two two-dimensional (2-D) detector arrays measuring in the spectral regions from 770 to 980 cm^{-1} (band A) and from 1070 to 1650 cm^{-1} (band B), respectively. Each 2-D detector array will consist of about 100×100 pixels, providing about 10 000 limb-views in the altitude range from 5 to 55 km and with a swath width of 320 km simultaneously. To increase the signal-to-noise ratio, individual array pixels will be co-added to obtain sampling patterns of specific scientific measurement modes.

Limb sounding exploits the radiation thermally emitted in the atmosphere along the line-of-sight (LOS) of the instrument, which is directed towards the limb of the Earth's atmosphere. The point of the LOS closest to the surface is called the tangent point. Under optically-thin conditions, the tangent point of the LOS generally determines the point in the atmosphere that contributes most to the measured radiation. The radiance of a single measurement typically originates mainly from an air volume with about 500 km extent along the LOS (half width of horizontal weighting function). The vertical

extent is mainly determined by the special viewing geometry of the limb observation and the vertical field-of-view (FOV), which has has about 750 m full-width at half-max (FWHM) at the tangent point. See Sect. 4.2 for a more detailed discussion of the two-dimensional radiative transfer weighting functions.

5   The main advantage of the proposed instrument concept is its great flexibility, i.e. the trade-off between spatial and spectral resolution can be adapted to the scientific needs. In this paper we will concentrate on the IRLS dynamics mode. It is designed to measure a subset of atmospheric variables with very high spatial sampling but moderate spectral sampling. Spectral sampling requirements are relaxed to 1.25 cm^{-1}. As an example,
10   simulated spectra for the IRLS dynamics mode for mid-latitude atmospheric conditions and 30 km tangent altitude are shown in Fig. 1. Even at reduced spectral resolution, infrared emission features of important atmospheric constituents (e.g. CO_2, O_3, HNO_3, CH_4, or N_2O) are clearly visible.

      The vertical coverage of the IRLS dynamics mode observations is 48 km with a lower
15   boundary that increases from 3 km at the poles to 7 km at the equator to account for the latitudinal variation of the tropopause height. Vertical sampling is 500 m. Limb images will be measured rearward to the flight direction of the satellite. Dense sampling along track is achieved by high measurement speed, i.e. about 7.5 s per image in the dynamics mode, corresponding to ≈50 km along track distance. The 2-D detector ar-
20   ray will allow for 13 parallel measurement tracks. The across track sampling is 25 km and the swath width is 320 km. The three-dimensional measurement grid of the PRE-MIER IRLS dynamics mode is illustrated in Fig. 2. The green spheres represent the tangent points of all measurements of a single image. Each blue orb represents a single measurement profile of preceding and following images, providing a visual clue for
25   the horizontal measurement density. Please note that tangent points of a single image are not placed vertically above one another as higher tangent points are located closer to the satellite; in fact, consecutive images are spaced so closely that the topmost tangent points of one image are placed vertically above the lowermost tangent points of the previous image.

Title Page

Abstract   Introduction

Conclusions   References

Tables   Figures

|◄   ►|

◄   ►

Back   Close

Full Screen / Esc

Printer-friendly Version

Interactive Discussion

In this study we are interested in determining the achievable resolution of the dynamics mode with a focus on resolving GWs. As the across track resolution directly corresponds to the across track sampling, it suffices to examine a single track and determine its resolution in vertical and along track direction. Further, we examine how well monochromatic GW waves can be reproduced by PREMIER measurements and tomographic retrieval techniques in accordance with one of the major scientific mission objectives.

3 Simulation setup

We examine how well tomographic temperature retrievals using simulated PRE-MIER IRLS dynamics mode measurements are able to reproduce GW parameters like amplitude, horizontal and vertical wavelength, as well as phase shifts. To this end, we carry out linear and non-linear retrieval end-to-end tests. We first simulate the radiance observations the PREMIER IRLS would make for a given monochromatic GW field. Second, we use the simulated observations to perform a tomographic temperature retrieval. Finally, retrieved temperatures are compared with the original field. We do not add noise or other instrument effects to the simulations as to not obscure the principal capacities of the approach; however, we do provide error estimates for retrieval noise.

The set of simulated measurements is designed according to the PREMIER specification as described in Sect. 2. For our analysis of the GW observational filter, we only use limb profiles of the central track of the 2-D array (depicted as red orbs in Fig. 2). In total 101 consecutive profiles along track with 91 measured altitudes each are used per simulation. The tangent point altitudes of one such profile range from 10 to 55 km spaced at intervals of ≈500 m. Figure 3 demonstrates how the line-of-sights of these dense measurements overlap one another in the along track direction. The same air volume is viewed from multiple viewing angles, which leads to a tomographic retrieval problem.

Tomographic retrieval approach for gravity wave observations

J. Ungermann et al.

Title Page

Abstract	Introduction
Conclusions	References
Tables	Figures

◄◄ ►►

◄ ►

Back Close

Full Screen / Esc

Printer-friendly Version

Interactive Discussion

To accurately represent a wide spectrum of GWs with different horizontal and vertical wavelength, we define a cross-section of the atmosphere 6000 km long and 82 km high. This accommodates the full LOS of 91 consecutive vertical measurement profiles of the central track constituting the measurement grid. For the initial calculation of simulated satellite measurements, this cross-section was finely gridded with a horizontal sampling of only 5 km and a vertical sampling of 50 m. For the retrieval of the baseline setup, we use a coarser sampling: the vertical sampling of the atmospheric retrieval grid corresponds to the measurement grid, i.e. 500 m between 10 km and 55 km height and 2 km outside this range. The horizontal sampling is set to 12.5 km (four times finer than the measurement grid) to avoid representation errors (see Sect. 6.2).

For other tracks than the central one, the tangent points of consecutive vertical measurement profiles do not lie within a plane. We therefore examined the effect of the angle of 2.6° between the LOS of the outermost tracks and the along track direction using both a 3-D atmosphere and a 2-D plane-parallel approximation and found the error of the approximation to be an order of magnitude smaller than the forward model error itself, i.e. to be negligible. In effect, the results presented below for the central track are representative for all tracks of the PREMIER IRLS.

We use typical mid-latitude atmospheric profiles from Remedios et al. (2007) as background for our input atmosphere and as "a priori" retrieval state. Onto this background and a priori atmosphere, waves with varying horizontal and vertical wavelength with a constant amplitude of 5 K are modulated to form the input atmospheres for our simulations; we refer to the latter atmospheres as "true" atmospheric state. Ideally, the retrieval would perfectly reproduce the true state.

4   Forward modelling

4.1   Fast forward model for the PREMIER IRLS

A fast and accurate radiative transfer model is essential to solve large inverse problems in atmospheric remote sensing. We adapted the Juelich Rapid Spectral Simulation Code (JURASSIC) (Hoffmann, 2006) for the PREMIER IRLS tomographic temperature retrievals presented in this paper. JURASSIC was previously used as forward model for retrievals for several satellite- and air-borne remote sensing experiments (e.g. Hoffmann et al., 2008, 2009). It was applied on dedicated GW studies for the Atmospheric Infrared Sounder aboard NASA's Aqua satellite (Eckermann et al., 2009; Hoffmann and Alexander, 2009). Specific code optimisations for the PREMIER performance assessment are outlined in Appendix A.

JURASSIC computes the radiative transfer based on the emissivity growth approximation (EGA) (Weinreb and Neuendorffer, 1973; Gordley and Russel, 1981; Marshall et al., 1994). Compared with conventional line-by-line calculations this approach is about a factor 1000 faster, since radiative transfer is calculated based on precalculated spectrally averaged values of emissivity stored in lookup tables. The emissivity look-up-tables for JURASSIC are prepared by means of exact line-by-line calculations utilising the Reference Forward Model (RFM) (Dudhia et al., 2002). In most stratospheric applications the EGA typically has an accuracy of 1 to 2% or better and no further means were taken here to improve forward model accuracy for the simulation study. Processing real measurements at a later stage may require improvements, e.g. by means of regression techniques (e.g. Francis et al., 2006).

JURASSIC provides a flexible handling of different types of observation geometries, e.g. nadir, sub-limb, limb, or zenith viewing for different types of atmospheric input data, e.g. single vertical profiles (1-D), sets of profiles along a satellite track (2-D), and regular or irregular 3-D model data. This is achieved by providing different interpolation functions for atmospheric data as well as a flexible 3-D ray-tracing routine (Hase and Höpfner, 1999).

Title Page

Abstract | Introduction

Conclusions | References

Tables | Figures

◄ | ►

◄ | ►

Back | Close

Full Screen / Esc

Printer-friendly Version

Interactive Discussion

For this project we apply a 2-D scheme with the grid described in Sect. 3. To sufficiently sample the atmospheric inhomogeneities along the ray paths the ray-tracing step length was set to a value of 0.4 km for generating the simulated measurements and 4 km for the actual retrieval. For pressure and aerosol extinction we apply a logarithmic vertical interpolation and a linear horizontal interpolation. Interpolation for temperature and trace gas volume mixing ratios is bi-linear.

Each measurement is affected by the vertical field-of-view of the instrument. A single radiative transfer calculation of JURASSIC however simulates an infinitesimal thin beam of radiation, also called a "pencil beam". To account for the effect of the FOV, we perform pencil beam calculations with a finer vertical sampling than that of the actual measurements. A single measurement is then simulated by convolving the results of the finely spaced pencil beam calculations with a sensitivity function describing the FOV of the instrument. We found a sampling two times as dense as the original measurement spacing to be sufficiently accurate, i.e. the tangentpoints of the pencil beams are vertically spaced at intervals of ≈ 250 m. Including pencil beams above and below the uppermost and lowermost measurement, we calculate 193 pencil beams for a single vertical measurement profile of the PREMIER IRLS consisting of 91 measurements.

4.2 Channel selection and weighting functions

For the temperature retrieval studies presented in this paper we analyse radiance emissions of the CO_2 Q-branch at 12.6 μm, which was successfully used by Riese et al. (1999) to retrieve stratospheric and mesospheric temperature distributions from satellite observations. Retrieving temperature from radiance measurements at individual spectral grid points of the PREMIER IRLS is technically feasible due to the rather low noise equivalent spectral radiance of the proposed instrument.

The temperature kernel functions presented here are computed by means of numerical perturbation. Figure 4 shows several kernel functions for the selected radiance channel at 12.6 μm (790.75 cm^{-1}). To analyse the temperature kernel functions

and provide a fast analytical representation for other studies, we developed a semi-empirical model. Preusse et al. (2002) provides an analytical model under the assumption of an optically transparent atmosphere. Our simulations indicate that in the 12.6 μm CO_2-branch transmittance gets as low as 0.6 and cannot be neglected. We therefore modified the model of Preusse et al. (2002) by adding a term compensating for transmittance. Here, the sensitivity of the measured signal on temperature at given altitude z (measured from the ground) and along track distance x (measured from the tangent point) is obtained from a Gaussian,

$$K(x,z)=K_0\exp\left[-\frac{(x-\mu)^2}{2\varphi_x^2}-\frac{(z-z_{t-x}^2/2R_E)^2}{2\varphi_z^2}\right].\tag{1}$$

Here K_0 denotes the maximum sensitivity. Note that the absolute values of K_0 presented below depend on the atmospheric grid sampling. The sensitivity will change when the grid sampling varies because the individual perturbations refer to smaller or larger air volumes. The standard deviations φ_z and φ_x measure the vertical extent of the weighting function as well as their extent along the LOS. The horizontal shift μ was introduced to deal with atmospheres, which are not optically thin as occurs in our setup. As kind of first-order effect, the point of maximum sensitivity will shift towards the instrument. In the exponential function, z_t denotes the tangent altitude. The term $-x^2/2R_E$, with Earth radius R_E, determines the apparent curvature of the ray paths with respect to the ground-base altitude coordinate system (Preusse et al., 2002).

We fitted the semi-empirical model to the temperature kernel functions shown in Fig. 4 to obtain statistics of the variables K_0, μ, φ_x, and φ_z. From 10 to 55 km altitude the maximum sensitivity K_0 decreases from 4×10^{-6} to 2×10^{-7} (W/(m^2 sr cm^{-1}))/K, the horizontal shift $-\mu$ towards the instrument decreases from 140 to 40 km, the horizontal full-width at half-max $2\sqrt{2\ln2}\varphi_x$ decreases from 575 to 475 km and the vertical full-width at half-max $2\sqrt{2\ln2}\varphi_z$ is nearly constant at 0.95 km. The semi-empirical model provides a reasonable description of the true kernel functions as the accuracy of the fits is about 2 to 3% of K_0.

5 Tomographic temperature retrieval

5.1 Inversion technique

Deriving atmospheric temperature values from (tomographic) infrared spectral measurements with poses a non-linear, ill-posed inversion problem (Hadamard, 1902). To obtain a unique and physically reasonable solution the problem needs to be regularised.

To perform the inversion, the JURASSIC retrieval processor implements a number of standard methods, of which the maximum a posteriori estimation (MAP) was selected (Rodgers, 1976). This method interprets measurements and atmospheric states statistically and determines an optimal weighted mean between an a priori atmospheric state and the measurements.

Let $n \in \mathbb{N}$ be the number of atmospheric state vector elements and $m \in \mathbb{N}$ the number of measurements. With $x_a \in \mathbb{R}^n$ being the a priori state of the atmosphere, $\mathbf{S_a} \in \mathbb{R}^{n \times n}$ a covariance matrix for x_a, $y \in \mathbb{R}^m$ the vector of measurements and $\mathbf{S}_\epsilon \in \mathbb{R}^{m \times m}$ the covariance matrix of the measurement error, effectively the cost function $J(x)$ with

$$J(x) = \left((x - x_a)^T \mathbf{S_a}^{-1} (x - x_a) + (F(x) - y)^T \mathbf{S}_\epsilon^{-1} (F(x) - y) \right) \qquad (2)$$

needs to be minimised to obtain the MAP solution. The minimisation is performed using the iterative Gauss-Newton algorithm. The resulting iteration formula can be written in two forms, one that requires the inverse of the covariance matrices and the solution of a linear equation system with n unknowns in each iteration (n-form), or one that requires solely the covariance matrices and the solution of a linear equation system with m unknowns in each iteration (m-form) (Rodgers, 2000). The choice of the more efficient form for our problem is critical since the linear algebra determines the memory consumption and thereby the maximal problem size. In our simulations m is generally much smaller than n, so we chose the m-form to reduce memory consumption and processing time.

Title Page

Abstract | Introduction

Conclusions | References

Tables | Figures

◄◄ | ►►

◄ | ►

Back | Close

Full Screen / Esc

Printer-friendly Version

Interactive Discussion

As initial guess or starting point $x_0 \in \mathbb{R}^n$ we selected the true atmospheric state to reduce simulation time. As this choice may sidestep potential convergence issues, it was confirmed for selected non-linear retrievals that they also converge to the same solution from other starting points, e.g. a polar atmosphere. Using a different starting point approximately doubles the number of required iteration steps. The covariance matrix $\mathbf{S}_e$ is assumed to be diagonal and takes into account noise (1 nW/(cm^2 sr cm^{-1})) as well as the quasi-statistical part of the forward model errors (which is estimated to be 0.3% of radiance, e.g. Hoffmann, 2006). The covariance matrix $\mathbf{S}_a$ is set up according to a first-order autoregressive model

$$(\mathbf{S}_a)_{i,j} = \sigma_i \sigma_j e^{-\frac{|v_i - v_j|}{c_v}} e^{-\frac{|h_i - h_j|}{c_h}}, \tag{3}$$

with v_i being the height of an atmospheric grid point and h_i its horizontal coordinate given as along track displacement in kilometres. The vertical correlation length c_v is chosen to be 0.5 km and the horizontal correlation length c_h is chosen to be 200 km (see Sect. 6.3 regarding the choice of value for these parameters). The variances σ_i are taken from the reference atmosphere of Remedios et al. (2007)

Only temperature values at grid points between 10 km and 65 km are retrieved, the others are fixed to the a priori atmosphere. Thereby an additional 10 km are retrieved compared to the uppermost tangent point height of 55 km.

Simulations of the JURASSIC forward model can be represented as the application of a function $F : \mathbb{R}^n \rightarrow \mathbb{R}^m$. Then $F'(x_i)$ is the Jacobian of the forward model F at atmospheric state $x_i \in \mathbb{R}^n$, also known as Kernel matrix. Each iteration step generates a new atmospheric state x_{i+1}

$$x_{i+1} = x_a + \mathbf{S}_a F(x_i)^T \left(F'(x_i) \mathbf{S}_a F'(x_i)^T + \mathbf{S}_e \right)^{-1} \cdot (y - F(x_i) + F'(x_i)(x_i - x_a)), \tag{4}$$

converging onto the optimal estimate $\hat{x} \in \mathbb{R}^n$.

The approach outlined above is traditionally applied to retrieve single vertical profiles of atmospheric data, but it is just as well-suited for 2-D tomographic retrieval problems,

Tomographic retrieval approach for gravity wave observations

J. Ungermann et al.

Title Page

Abstract | Introduction

Conclusions | References

Tables | Figures

◄ | ►

◄ | ►

Back | Close

Full Screen / Esc

Printer-friendly Version

Interactive Discussion

the only difference being the interpretation of the state vector x_i. Please note that we do not apply a sequential approach based on retrievals of individual profiles like described by Steck et al. (2005), but solve the full 2-D problem.

Figure 5 shows exemplarily the results from such an end-to-end test. The temperature perturbation of the input atmosphere is depicted in Fig. 5b. The tangent points of measurements are shown as white circles. The outcome of the retrievals is shown if Fig. 5c). One can clearly see that the wave structure is qualitatively well reproduced between 10 and 55 km height. In the area between 55 km and 65 km, the wave structure degrades into the a unperturbed priori atmosphere due to a lack of measurement information. The amplitude of the retrieved wave sometimes slightly surpasses ±5 K, which is shown as white areas in the wave trough and crest. Figure 5d) depicts the difference between the input atmosphere and the result; the error is overall less than 0.5 K between 20 and 50 km height.

5.2 Characteristics and error analysis

5.2.1 Measurement contribution and resolution

The averaging kernel matrix $\mathbf{A} \in \mathbb{R}^{n \times n}$ of the final estimate $\hat{x}$

$$\mathbf{A} = \mathbf{S_a} F'(\hat{x})^T \left(F'(\hat{x}) \mathbf{S_a} F'(\hat{x})^T + \mathbf{S_\epsilon} \right)^{-1} F'(\hat{x}). \tag{5}$$

describes the characteristics of the retrieval.

One row of the averaging kernel matrix of the baseline setup with no modulated wave structure is depicted in Fig. 6. As each element in the row describes the influence of one point of the true atmosphere on the result, it can be reordered two-dimensionally according to their horizontal and vertical coordinates. The figure is representative for rows belonging to measurements with tangent points located between 15 km and 50 km height. Aside from a strong centred peak, one can see small "ripples" in the vicinity of the peak resembling the shape of the weighting functions (compare with Fig. 4). The asymmetry is caused by the asymmetry of the weighting functions.

Using the averaging kernels it is possible to deduce measurement contribution and resolution of the retrieval. Typical values are plotted in Fig. 7. The contribution of measurement information to the retrieval results is estimated by calculating the area below the rows of the averaging kernel matrix. The tangent points of measurements lie within the region of 10 to 55 km height and 500 to 5500 km horizontal distance, which closely corresponds to the region where the measurement contribution in Fig. 7a is between 0.95 and 1.05. Outside this region retrieval results are dominated by a priori information. As we are mainly interested in results with high measurement content and to simplify data processing, only data points with a measurement contribution between 0.95 and 1.05 are evaluated further.

The averaging kernels can also be used to estimate vertical and horizontal resolution by mapping each row of the averaging kernel matrix associated with an atmospheric sample to the two-dimensional structure it represents as is depicted in Fig. 6. In this form, the FWHM of the vertical respectively horizontal direction can be calculated (e.g. Steck et al., 2005; von Clarmann et al., 2009). Figure 7b and 7c show exemplarily the estimated horizontal and vertical resolution. As can be seen in Fig. 6, the averaging kernels generally contain numerous very small elements that describe the influence of atmospheric sample points that are not directly above or beside the atmospheric sample point in question; as these are disregarded when calculating the resolution, this method provides an approximate measure of resolution.

The vertical resolution in the central area is slightly better than the assumed vertical FOV, which has a FWHM of 750 m; however, without the effects of the a priori vertical correlation a vertical resolution of nearly 500 m, corresponding to the vertical sampling of measurements, is achievable (see Sect. 6.3). This shows that the achievable resolution is not necessarily limited by the FOV. The horizontal resolution of about 70 km comes close to the measurement grid sampling (50 km) and is a significant improvement compared to the 475 to 575 km FWHM of the individual weighting functions. Combined with the across track sampling and resolution of 25 km, PREMIER IRLS is the first limb sounder with a horizontal resolution comparable to nadir sounders.

The simulations indicate that spatially over-sampled measurements (with respect to the weighting functions) can be separated and provide high spatial resolution in the vertical and horizontal domain.

5.2.2 Retrieval noise

The effect of noise on the retrieval can be estimated based on the effect of perturbations of the measurements on the retrieval result.

As our a priori covariance matrix for the atmospheric state is not derived from a climatology, but chosen ad-hoc, the retrieval covariance matrix should not be interpreted statistically. Instead, we use the retrieval noise for diagnosis, i.e. the effect of measurement noise on the retrieval result. The gain matrix $\mathbf{G} \in \mathbb{R}^{n \times m}$, which maps the measurements into the atmospheric state space, is defined as

$$\mathbf{G} = \mathbf{S_a} F'(\hat{x})^T \left(F'(\hat{x}) \mathbf{S_a} F'(\hat{x})^T + \mathbf{S}_\varepsilon \right)^{-1}. \tag{6}$$

It can be used to estimate the retrieval noise covariance matrix:

$$\mathbf{S_{noise}} = \mathbf{G} \mathbf{S}_\varepsilon \mathbf{G}^T. \tag{7}$$

The retrieval noise is the most important error for gravity wave analysis as the effect of other, systematic errors can be more readily handled by detrending. It will be analysed and compared with GW amplitudes in Sect. 6.3.

6 Gravity wave observational filter

The observational filter defines how a wave perturbation of given horizontal and vertical wavelength is reproduced by a retrieval. The retrieval may modify the wave amplitude, wavelength, and phase in a complicated way. As the amplitude is the most important feature of the wave with respect to its energy, the assessment presented here focuses on how well the amplitude of a given wave is reproduced.

Tomographic retrieval approach for gravity wave observations

J. Ungermann et al.

6.1 Deduction from end-to-end simulations

To determine the observational filter, end-to-end simulations must be performed for all waves of interest. To deduce the amplitude of the wave in the retrieved atmosphere, all atmospheric grid points between 15 and 50 km and along track 1500 to 4500 km are fitted against the modulated wave with amplitude as the only free parameter using a least-square fit. Please note that this does not compensate for eventual shifts in phase as is generally present in 1-D retrievals (Preusse et al., 2009); any phase shift present would reduce the sensitivity (even to zero for a phase shift of 180°). However, tests including the phase shift in the fit indicated that no phase shift was present. According to Shannon's sampling theorem, it is impossible to perfectly reproduce waves with wavelength δ using a sampling distance longer than $\delta/2$; for this reason we tested only waves from a vertical wavelength of 1 km upwards and from a horizontal wavelength of 100 km upwards.

Figure 8a shows the filter for the baseline setup described in Sect. 3; it corresponds qualitatively with the shape of analytically derived sensitivity of Preusse et al. (2002), albeit most notably the region of good sensitivity is moved well towards shorter horizontal wavelengths. Due to the much denser atmospheric sampling and the tomographic approach, much smaller waves become visible. The finest horizontal wavelength resolvable is about 100 km for a vertical wavelength around 5 km running towards the instrument. This is a significant improvement compared to the roughly 250 km horizontal wavelength of previous sensitivity studies involving the CRISTA instrument (Preusse et al., 2002). Please note that the resolvable horizontal wavelength is much smaller than the horizontal FWHM of the weighting function, which is roughly 500 km. Waves of a vertical wavelength of 2 km can be retrieved well, but the sensitivity drops quickly for shorter vertical wavelengths, as the measurement grid is not fine enough to properly resolve them. Around two kilometre vertical wavelength and long horizontal wavelength, the retrieved amplitude becomes slightly larger than 1; this is caused by an insufficient vertical sampling of the atmospheric retrieval grid, similar to the horizontal

sampling issue discussed below in Sect. 6.2 but less pronounced. For waves with large vertical wavelength, the sensitivity becomes smaller depending strongly on the horizontal wavelength. But for waves with 300 km horizontal wavelength and longer, a sensitivity of at least 0.5 is given for all examined vertical wavelength longer than 2 km.
5 Sensitivity rises to 1 for all waves with horizontal wavelength longer than ≈500 km (not shown).

Varying the phase of the modulated wave had no significant influence on the sensitivity filter derived by the 2-D retrieval and is therefore not depicted. Small differences are present for waves with vertical wavelength below 2 km where the resolvability strongly
10 depends on the relation between wave peaks and sampling grid. Changing the orientation of the waves from running towards the instrument to running away from it has a significant influence as is shown in Fig. 8b. The sensitivity to waves with a horizontal wavelength below 150 km is lost, but this is compensated by an increased sensitivity to waves with a larger vertical wavelength and an overall smaller transition region, in
15 which waves become distorted. As the atmosphere is not completely transparent, the sensitivity of the ray to temperature changes is not only a function of height, but also of the horizontally travelled distance, which can be clearly seen in Fig. 4. As the sensitivity to waves largely depends on the relation between ray path and wave trough and crest (Preusse et al., 2002) this is to be expected and needs to be taken into account
20 when GW parameters are deduced from retrieved temperatures.

6.2 Sensitivity to retrieval grid sampling

The horizontal sampling of the retrieval grid has a significant influence on the retrieval results as shown in Fig. 8c.

Before settling on a horizontal sampling distance of 12.5 km for the retrieval grid,
25 several other sampling grids were tested ranging from 6.75 km to 400 km. It was found that the larger the sampling distance became, the more pronounced the amplification of wave amplitudes for short GW lengths became. This amplification can be seen in Fig. 8c), which depicts the filter for a "natural" retrieval grid being identical with the

measurement grid. Apparently at least for GW with short wavelengths, the natural sampling is not necessarily the best choice.

The amplification of retrieved waves is most likely caused by the bi-linear interpolation of the temperature between the grid points. The fine structure of wave perturbations with short wavelength cannot be sufficiently represented by linear interpolation, which the retrieval compensates for by raising the wave amplitudes. Therefore, either a different atmospheric representation more suited to represent wave structures is needed or the grid sampling needs to be refined to sufficiently capture the variations of the atmospheric state. Here we employ the second approach. If the retrieval grid sampling drops below the measurement grid sampling, the problem becomes underdetermined and needs to be regularised appropriately. Simulations have shown that resolution, measurement content and retrieval noise are not noticeably impacted by the refinement of the atmospheric grid.

For the examined waves, the artificial amplitude magnification is greatly diminished with a horizontal grid distance of 25 km and negligible at 12.5 km. The sampling distance of 12.5 km was chosen to obtain exactness of the results.

As mentioned in Sect. 6.1, a similar effect occurs for waves with small vertical wavelength, which increases the retrieved amplitude by an factor of up to 1.2 for waves with about 2 km vertical wavelength. As the effect is much less pronounced and therefore easier to correct, we decided not to increase the vertical retrieval grid sampling for this study.

6.3 Tradeoff between retrieval noise and resolution

The vertical and horizontal correlation length of the a priori covariance plays the most important role in the MAP regularisation applied here. Different values were examined before the values of 0.5 km and 200 km were chosen to provide a satisfactory trade-off between resolution and retrieval noise.

Title Page

Abstract | Introduction

Conclusions | References

Tables | Figures

◀ | ▶

◀ | ▶

Back | Close

Full Screen / Esc

Printer-friendly Version

Interactive Discussion

Figure 9 shows the effect of the vertical correlation length on vertical resolution and retrieval noise. To decrease the retrieval noise to ≈0.5 K for most of the vertical range, while still retaining a good vertical resolution, a correlation length of 0.5 km was finally chosen. The choice of vertical correlation parameter also influences the GW observa-
tional filter. As expected, a large correlation length slightly reduces the region where sensitivity is very close to one. We further found that increasing the vertical correlation length beyond 2 km leads to unwanted oscillations in the averaging kernels, which confirms our choice of a much smaller value.

The retrieval noise is not influenced significantly by the horizontal correlation fac-
tor we examined (12.5 to 400 km) and therefore not depicted. The main effect of the horizontal correlation is to stabilise the underdetermined retrievals. Reducing the hor-
izontal correlation length from 200 km to 100 km improves the horizontal resolution from 75 km to ≈70 km, but the non-linear retrievals do not converge for some wave structures with very small vertical and horizontal wavelength. Reducing the horizontal
correlation further, the horizontal resolution derived from the averaging kernel matrix goes as low as 50 km for a horizontal correlation length of 12.5 km, i.e. is close to the horizontal measurement sampling grid at the cost of ever increasing convergence is-
sues. To avoid any convergence problems, a correlation length of 200 km was chosen. The GW observational filter behaves as expected when varying the horizontal corre-
lation length, as waves become increasingly dampened for larger correlation lengths. However, this barely affects the region of the GW observational filter close to one but influences mostly the transition region.

For GW analysis, it is important that the retrieval noise of the retrieval is smaller than the GW amplitude. According to the sampling theorem, with a vertical sampling grid
of 500 m one cannot resolve waves with a vertical wavelength being shorter than 1 km. Practically, a slightly larger vertical wavelength than 1 km is required, meaning that we expect to consistently resolve waves of about 2 km vertical wavelength, an expectation confirmed by the GW observational filter. The maximal amplitude of actual GWs of that vertical wavelength can be determined according to the temperature amplitude

saturation limit (e.g. Preusse et al., 2008). This limit $\hat{T}_{max}$ due to static instability is proportional to the vertical wavelength:

$$\hat{T}_{max} = \frac{\lambda_z}{2\pi}\frac{\overline{T}}{g}N^2. \tag{8}$$

Using $N = 0.02\,\text{s}^{-1}$ and a background temperature $\overline{T}$ of 250 K, this gives a saturation
5 amplitude of greater than 3.2 K for waves with vertical wavelength greater than or equal to 2 km at about 40 km height. Comparing this value to the 0.5 K of retrieval noise for that height range shows that such GWs are well detectable also in the presence of noise. As the temperature amplitude saturation limit increases with vertical wavelength, any wave with vertical wavelength longer than 2 km is therefore also detectable with the
10 given noise level.

6.4 Deducing the gravity wave observational filter from the averaging kernel matrix

A more efficient way to derive the GW observational filter is to analyse the averaging kernel matrix of a retrieval for a climatological atmosphere of the region of interest.
15 Assuming the non-linearities of the forward model to be negligible and thereby the Jacobian to be constant across the space spanned by the a priori atmosphere and all examined wave perturbations, the averaging kernel matrix **A** will be identical for all wave structures and the unperturbed atmosphere. Neglecting measurement errors, it follows that

20 $\hat{x} - x_a = (\mathbf{A}(x_a + x_\delta) + (\mathbf{I}-\mathbf{A})x_a) - x_a = \mathbf{A}x_\delta,$ (9)

with x_δ being the modulated wave structure. This shows that the averaging kernel matrix directly maps the true wave perturbations x_δ onto the retrieved wave structure.
Figure 10 shows the GW observational filter derived in this manner. Just as for the non-linear end-to-end simulations, only the part of the $\hat{x} - x_a$ vector is used to derive

Title Page

Abstract · Introduction

Conclusions · References

Tables · Figures

◄ · ►

◄ · ►

Back · Close

Full Screen / Esc

Printer-friendly Version

Interactive Discussion

the sensitivity that has a good measurement contribution and lies well within the region covered by tangent points of measurements. The perturbations of up to 5 K are small enough that the assumption about linearity of the forward model sufficiently holds. The filter derived in this manner replicates closely the structure of the filter derived from
5 non-linear end-to-end tests.

This method is therefore an efficient way to quickly evaluate the effect of changes in the setup before proceeding to the much more computational intensive non-linear end-to-end simulations.

6.5 Comparison of 2-D and 1-D retrievals

10 A 2-D retrieval reproduces wave structures with better sensitivity and less distortions than 1-D retrievals assuming a homogeneously stratified atmosphere.

For example, Fig. 11 shows side-by-side the retrieval results for a wave of 320 km horizontal wavelength and 30 km vertical wave length. Figure 11a was generated by a series of 1-D retrievals, each using a single vertical measurement profile of the sim-
15 ulated measurements as input. The resulting temperature profiles were assembled to a 2-D structure by adding each retrieved temperature profile at the mean horizontal location of the tangent points of the involved measurements. The phase of the wave structure of the 1-D retrieval is disturbed by about 180°; the amplitudes do not surpass 2 K and are thereby much smaller than the expected 5 K. In addition, the amplitude has
20 also a strong artificial height-dependence. The vertical wavelength is also slightly reduced. On the other hand, the 2-D retrieval shows a more pronounced wave structure and fits well to the true wave (not depicted) in the region between 25 km and 55 km; the 2-D retrieval deviates less than 2 K from the true atmospheric state whereas the 1-D retrieval is subject to deviations of more than 6 K (the latter is partly caused by the
25 180° phase shift). As depicted in Fig. 8, this retrieval has an amplitude dampening factor of 0.9.

The GW observational filter deduced using 1-D retrievals is shown in Fig. 11c. In contrast to Fig. 8, also the phase of the wave was fitted (not depicted), otherwise the

sensitivity would be even worse. It is apparent that fewer wave patterns can be reliably retrieved. Especially waves with large vertical wavelength are affected. This comparison shows that tomographic retrievals are superior for the purpose of GW detection.

7 Summary and conclusions

We performed various non-linear end-to-end simulations using simulated measurements of the PREMIER IRLS with different input atmospheres consisting of a climatological background atmosphere with modulated wave perturbations. In this way, we determined the gravity wave (GW) observational filter that shows the amplitude with which a given wave perturbation is reproduced by our tomographic retrieval setup. It was shown that the new, innovative PREMIER IRLS using the dense measurement grid of the dynamics mode combined with tomographic retrievals can resolve much finer GW structures than previously possible. GW with a horizontal wavelength down to 100 km may be resolved depending on the vertical wavelength.

We examined different retrieval grids and found that using a coarse retrieval grid introduces an amplification of GWs with short wavelength. It is therefore essential to use a retrieval grid that is sufficiently fine for the purpose of representing examined and existing atmospheric structure. Otherwise, retrieval results may be tainted by artifacts.

By tweaking the correlation length of the a priori covariance matrix, it is possible to reduce the retrieval noise at the cost of a reduced resolution. We also found that convergence issues arise when the horizontal correlation length is reduced to or below 100 km. We examined various horizontal and vertical correlation length and settled for a horizontal correlation length of 200 km and a vertical correlation length of 0.5 km. With these figures, the expected retrieval noise is well below the temperature amplitude saturation limit of resolvable GWs.

A linear approximation of the observation filter derived from the averaging kernel matrix is a helpful tool when examining different setups. One may generate the averaging kernel matrix for a climatological atmosphere and use this to inexpensively calculate

an approximation of the observation filter for a wide range of GWs. The observational filter derived in this manner resembles closely the observational filter derived by more accurate end-to-end simulations including the distinction between GW running towards or away from the satellite.

The observational filter derived by conventional 1-D retrievals has a severely reduced sensitivity compared to the observational filter derived by our tomographic retrieval technique. Comparing the results for selected wave perturbations, we found the result of the tomographic retrieval to be much closer to the true state than the result of the 1-D retrieval. Further, the tomographic retrieval is not subject to the massive shift in phase that affects 1-D retrievals.

The PREMIER IRLS will provide 3-D temperature measurements with sufficient altitude coverage and resolution in the stratosphere to allow for simultaneous determination of GW temperature amplitudes and the associated horizontal and vertical wavelength. Therefore, the dynamics mode of the PREMIER satellite instrument is well suited for examining the dynamic structure of the atmosphere. The presented tomographic retrieval scheme resolves the dense 3-D measurement of the PREMIER IRLS dynamics mode with a comparable 3-D resolution and is thereby well suited for the retrieval of temperature data for the analysis of GWs. The across track resolution of PREMIER IRLS corresponds to the across track sampling of 25 km. Further, it is possible to retrieve temperature data with a vertical resolution of 750 m; depending on the retrieval setup even a vertical resolution of 500 m is achievable, surpassing the full-height-at-half-maximum of the vertical field-of-view (750 m). In addition, one can nearly fully exploit the dense measurement grid of 50 km horizontal distance with an achievable horizontal along track resolution of $\approx$70 km, which is unprecedented for LIMB sounders and for the first time approaches the horizontal resolution of NADIR sounders.

Appendix A

Code optimisation and performance

Conventional 1-D retrievals often depend on the assumption of horizontal homogene-
ity to represent the atmosphere by a single profile. For tomographic retrievals this
assumption is discarded, requiring a much larger number of variables to properly rep-
resent the atmosphere. Combined with an increased number of measurements, the
retrieval process becomes technically more demanding. To enable many such retrieval
simulations, the JURASSIC forward model and the retrieval processor were optimised
both for modern imager instruments and tomographic retrievals.

The first change improved the calculation speed of the Jacobians involved in the
retrieval, which JURASSIC calculates using a finite differences approach. For tomo-
graphic retrievals, a single ray path crosses only a minor fraction of points of the full
atmospheric grid, which results in rather sparse Jacobians compared to 1-D retrievals.
For the specific PREMIER setup only between one and three percent of the entries
of the Jacobian matrix are non-zero. By generating a data structure that tracks which
points of the atmosphere influence which pencil beams, it is possible to simply skip
the calculation of pencil beams unaffected by the current perturbation. In effect, zeros
within the Jacobian cost next to no processing time. Further, generally, only part of
the pencil beams influencing a single changed measurement need to be recalculated,
resulting in an overall speedup of ≈ 200 for the type of problems considered here.

The second change involved reworking the linear algebra of the retrieval processor.
For conventional 1-D retrievals, the processing time spent in the matrix multiplications
and equation system solving is irrelevant compared to the calculation of the Jacobians.
For increased problem sizes, it becomes much more important, beginning to noticeably
increase the processing time and to dominate the memory consumption. Using sparse
representations of the Jacobian matrices, more efficient algorithms to solve the linear
equation systems and the Automatically Tuned Linear Algebra Software (ATLAS) BLAS

Tomographic retrieval approach for gravity wave observations

J. Ungermann et al.

Title Page

Abstract	Introduction
Conclusions	References
Tables	Figures

⏮   ⏭

◀   ▶

Back   Close

Full Screen / Esc

Printer-friendly Version

Interactive Discussion

implementation by Whaley et al. (2001), could halve the previous memory consumption and significantly reduce the processing time.

For our simulations, a cluster of 16 compute nodes is used, each fitted with 64 Gb RAM and two AMD Quad-Core Opteron 2380 CPUs. To retrieve the baseline setup (19 493 pencil beams combined to 9191 measurements for retrieving 46 080 atmospheric state vector elements) with a single thread, roughly seven hours are needed. A simple OpenMP parallelisation of the embarrassingly parallel forward model together with the multi-threaded ATLAS backend allows a faster execution on a multi-core host. Figure 12 shows the speedup realised with the OpenMP parallelisation. From the curve can be deduced that about 93% of the retrieval code are parallelised.

Acknowledgements. We sincerely thank A. Dudhia, Uni. Oxf., for providing us with the reference forward model (RFM).

References

Adams, S., Spang, R., Preusse, P., and Heinemann, G.: The benefit of limb cloud imaging for infrared limb sounding of tropospheric trace gases, Atmos. Meas. Tech., 2, 287–298, 2009, http://www.atmos-meas-tech.net/2/287/2009/. 2811

Alexander, J.: Interpretations of observed climatological patterns in stratospheric gravity wave variance, Geophys. Res. Lett., 103, 8627–8640, 1998. 2813

Alexander, J. and Rosenlof, K. H.: Gravity-wave forcing in the stratosphere: Observational constraints from the Upper Atmosphere Research Satellite and implications for parameterization in global models, Geophys. Res. Lett., 108, 4597, doi:10.1029/2003JD003373, 2003. 2812

Carlotti, M., Dinelli, B. M., Raspollini, P., and Ridolfi, M.: Geo-fit approach to the analysis of limb-scanning satellite measurements, Appl. Optics, 40, 1872–1885, 2001. 2812

Carlotti, M., Brizzi, G., Papandrea, E., Prevedelli, M., Ridolfi, M., Dinelli, B. M., and Magnani, L.: GMTR: Two-dimensional geo-fit multitarget retrieval model for Michelson Interferometer for Passive Atmospheric Sounding/Environmental Satellite observations, Appl. Optics, 45, 716–727, 2006. 2812

Drummond, J. R., Houghton, J. T., Peskett, G. D., Rodgers, C. D., Wale, M. J., Whitney, J., and

Williamson, E. J.: The stratospheric and mesospheric sounder on Nimbus 7, Philos. T. R. Soc. Lond., 296, 219–241, 1980. 2811

Dudhia, A., Morris, P. E., and Wells, R. J.: Fast monochromatic radiative transfer calculations for limb sounding, J. Quant. Spectrosc. Ra., 74, 745–756, 2002. 2817

Dunkerton, T.: The role of gravity waves in the quasi-biennial oscillation, J. Geophys. Res., 102, 26053–26076, 1997. 2812

Eckermann, S. D. and Preusse, P.: Global measurements of stratospheric mountain waves from space, Science, 286, 1534–1537, 1999. 2812

Eckermann, S. D., Hoffmann, L., Höpfner, M., Wu, D. L., and Alexander, M. J.: Antarctic NAT PSC belt of June 2003: Observational validation of the mountain wave seeding hypothesis, Geophys. Res. Lett., 36, L02807, doi:10.1029/2008GL036629, 2009. 2817

Ern, M., Preusse, P., Alexander, M. J., and Warner, C. D.: Absolute values of gravity wave momentum flux derived from satellite data, J. Geophys. Res., 109, D20103, doi:10.1029/2004JD004752, 2004. 2812, 2813

Ern, M., Preusse, P., and Warner, C. D.: A comparison between CRISTA satellite data and Warner and McIntyre gravity wave parameterization scheme: horizontal and vertical wavelength filtering of gravity wave momentum flux, Adv. Space Res., 35, 2017–2023, 2005. 2813

ESA: Candidate Earth Explorer Core Missions – Report for Assessment: PREMIER – PRocess Exploitation through Measurements of Infrared and millimetre-wave Emitted Radiation, SP-1313/5, ESA Publications Division, ESTEC, Keplerlaan 1, 2200 AG Noordwijk, The Netherlands, 2008. 2811, 2812

Fischer, H., Birk, M., Blom, C., Carli, B., Carlotti, M., von Clarmann, T., Delbouille, L., Dudhia, A., Ehhalt, D., Endemann, M., Flaud, J. M., Gessner, R., Kleinert, A., Koopman, R., Langen, J., López-Puertas, M., Mosner, P., Nett, H., Oelhaf, H., Perron, G., Remedios, J., Ridolfi, M., Stiller, G., and Zander, R.: MIPAS: an instrument for atmospheric and climate research, Atmos. Chem. Phys., 8, 2151–2188, 2008, http://www.atmos-chem-phys.net/8/2151/2008/. 2811

Francis, G. L., Edwards, D. P., Lambert, A., Halvorson, C. M., Lee-Taylor, J. M., and Gille, J. C.: Forward modeling and radiative transfer for the NASA EOS-Aura High Resolution Dynamics Limb Sounder (HIRDLS) instrument, J. Geophys. Res., 111, D13301, doi:10.1029/2005JD006270, 2006. 2817

Friedl-Vallon, F., Riese, M., Maucher, G., Lengel, A., Hase, F., Preusse, P., and Spang, R.: Instrument concept and preliminary performance analysis of GLORIA, Adv. Space Res., 37,

Tomographic retrieval approach for gravity wave observations

J. Ungermann et al.

2287–2291, 2006. 2811

Fritts, D. C. and Alexander, M. J.: Gravity wave dynamics and effects in the middle atmosphere, Rev. Geophys., 41, 1003, doi:10.1029/2001RG000106, 2003. 2812

Gille, J. C. and Russel III, J. M.: The Limb Infrared Monitor of the Stratosphere: Experiment
5 Description, Performance, and Results, J. Geophys. Res., 89, 5125–5140, 1984. 2811

Gordley, L. L. and Russel, J. M.: Rapid inversion of limb radiance data using an emissivity growth approximation, Appl. Optics, 20, 807–813, 1981. 2817

Hadamard, J.: Sur les problmes aux drives partielles et leur signification physique, Princeton University Bulletin, 49–52, 1902. 2820

10 Hase, F. and Höpfner, M.: Atmospheric ray path modeling for radiative transfer algorithms, Appl. Optics, 38, 3129–3133, 1999. 2817

Hertzog, A., Boccara, G., Vincent, R. A., Vial, F., and Coquerez, P.: Estimation of gravity-wave momentum flux and phase speeds from long-duration stratospheric balloon flights, 2: Results from the Vorcore campaign in Antarctica, J. Atmos. Sci., 65, 3056–3070, 2008. 2813

15 Hoffmann, L.: Schnelle Spurengasretrieval für das Satellitenexperiment Envisat MIPAS, Forschungszentrum Jülich, Germany, Tech. Rep. JUEL-4207, ISSN 0944-2952, 2006. 2817, 2821

Hoffmann, L. and Alexander, M. J.: Retrieval of stratospheric temperatures from Atmospheric Infrared Sounder radiance measurements for gravity wave studies, J. Geophys. Res., 114,
20 D07105, doi:10.1029/2008JD011241, 2009. 2812, 2817

Hoffmann, L., Kaufmann, M., Spang, R., Müller, R., Remedios, J. J., Moore, D. P., Volk, C. M., von Clarmann, T., and Riese, M.: Envisat MIPAS measurements of CFC-11: retrieval, validation, and climatology, Atmos. Chem. Phys., 8, 3671–3688, 2008, http://www.atmos-chem-phys.net/8/3671/2008/. 2812, 2817

25 Hoffmann, L., Weigel, K., Spang, R., Schroeder, S., Arndt, K., Lehmann, C., Kaufmann, M., Ern, M., Preusse, P., Stroh, F., and Riese, M.: CRISTA-NF measurements of water vapor during the SCOUT-O$_3$ Tropical Aircraft Campaign, Adv. Space Res., 43, 74–81, 2009. 2817

Livesey, N. J. and Read, W. G.: Direct Retrieval of Line-of-Sight Atmospheric Structure from Limb Sounding Observations, Geophys. Res. Lett., 27, 891–894, 2000. 2812

30 Marshall, B. T., Gordley, L. L., and Chu, D. A.: BANDPAK: Algorithms for Modeling Broadband Transmission and Radiance, J. Quant. Spectrosc. Ra., 52, 581–599, 1994. 2817

McLandress, C.: On the importance of gravity waves in the middle atmosphere and their parameterization in general circulation models, J. Atmos. Sol.-Terr. Phy., 60, 1357–1383, 1998.

Tomographic retrieval approach for gravity wave observations

J. Ungermann et al.

McLandress, C. and Shepherd, T. G.: Simulated anthropogenic changes in the Brewer-Dobson circulation, including its extension to high latitudes, J. Climate, 22, 1516–1540, 2009. 2812

Preusse, P., Eckermann, S. D., and Offermann, D.: Comparison of global distributions of zonal-mean gravity wave variance inferred from different satellite instruments, Geophys. Res. Lett., 27, 3877–3880, 2000. 2813

Preusse, P., Dörnbrack, A., Eckermann, S. D., Riese, M., Schaeler, B., Bacmeister, J. T., Broutman, D., and Grossmann, K. U.: Space-based measurements of stratospheric mountain waves by CRISTA, 1, Sensitivity, analysis method, and a case study, J. Geophys. Res., 107(D23), 8178, doi:10.1029/2001JD000699, 2002. 2812, 2819, 2825, 2826

Preusse, P., Eckermann, S. D., and Ern, M.: Transparency of the atmosphere to short horizontal wavelength gravity waves, J. Geophys. Res., 113, D24194, doi:10.1029/2007JD009682, 2008. 2829

Preusse, P., Schroeder, S., Hoffmann, L., Ern, M., Friedl-Vallon, F., Ungermann, J., Oelhaf, H., Fischer, H., and Riese, M.: New perspectives on gravity wave remote sensing by spaceborne infrared limb imaging, Atmos. Meas. Tech., pp. 299–311, 2009. 2812, 2825

Remedios, J. J., Leigh, R. J., Waterfall, A. M., Moore, D. P., Sembhi, H., Parkes, I., Greenhough, J., Chipperfield, M. P., and Hauglustaine, D.: MIPAS reference atmospheres and comparisons to V4.61/V4.62 MIPAS level 2 geophysical data sets, Atmos. Chem. Phys. Discuss., 7, 9973–10017, 2007,
http://www.atmos-chem-phys-discuss.net/7/9973/2007/. 2816, 2821, 2839

Riese, M., Spang, R., Preusse, P., Ern, M., Jarisch, M., Offermann, D., and Grossmann, K. U.: Cryogenic Infrared Spectrometers and Telescopes for the Atmosphere (CRISTA) data processing and atmospheric temperature and trace gas retrieval, J. Geophys. Res., 104, 16349–16367, 1999. 2811, 2818

Riese, M., Friedl-Vallon, F., Spang, R., Preusse, P., Schiller, C., Hoffmann, L., Konopka, P., Oelhaf, H., von Clarmann, T., and Höpfner, M.: GLObal limb Radiance Imager for the Atmosphere (GLORIA): Scientific objectives, Adv. Space Res., 36, 989–995, 2005. 2811

Rodgers, C. D.: Retrieval of Atmospheric Temperature and Composition From Remote Measurements of Thermal Radiation, Rev. Geophys. Space Ge., 14, 609–624, 1976. 2820

Rodgers, C. D.: Inverse Methods for Atmospheric Sounding: Theory and Practice, vol. 2 of Series on Atmospheric, Oceanic and Planetary Physics, World Scientific, 2000. 2820

Steck, T., Höpfner, M., von Clarmann, T., and Grabowski, U.: Tomographic retrieval of atmo-

Tomographic retrieval approach for gravity wave observations

J. Ungermann et al.

Title Page

Abstract	Introduction
Conclusions	References
Tables	Figures

◀◀   ▶▶

◀   ▶

Back   Close

Full Screen / Esc

Printer-friendly Version

Interactive Discussion

spheric parameters from infrared limb emission observations, Appl. Optics, 44, 3291–3301, 2005. 2812, 2822, 2823

von Clarmann, T., De Clercq, C., Ridolfi, M., Hopfner, M., and Lambert, J.-C.: The horizontal resolution of MIPAS, Atmos. Meas. Tech., 2, 47–54, 2009,
http://www.atmos-meas-tech.net/2/47/2009/. 2823

Weinreb, M. P. and Neuendorffer, A. C.: Method to Apply Homogeneous-path Transmittance Models to Inhomogenous Atmospheres, J. Atmos. Sci., 30, 662–666, 1973. 2817

Whaley, R. C., Petitet, A., and Dongarra, J. J.: Automated Empirical Optimization of Software and the ATLAS Project, Parallel Comput., 27, 3–35, 2001. 2834

Tomographic retrieval approach for gravity wave observations

J. Ungermann et al.

a)

b)
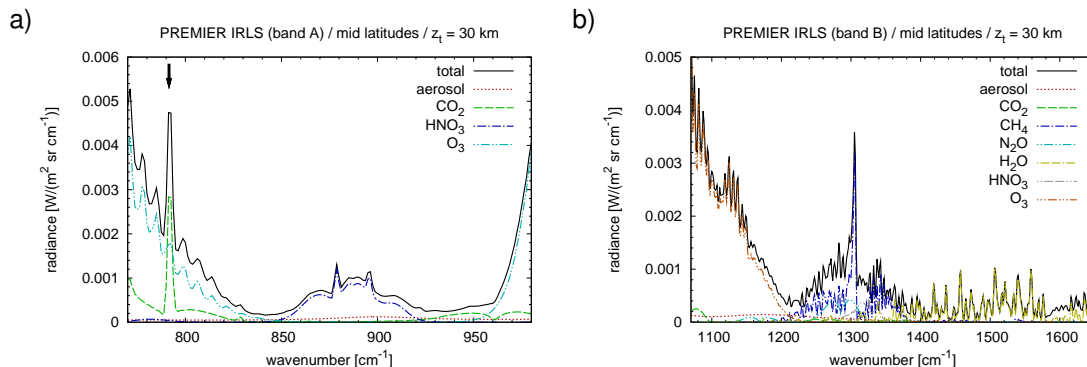
Fig. 1. Simulated radiance spectra for the PREMIER IRLS band A and B. Calculations are based on mid-latitude atmospheric conditions (Remedios et al., 2007) and 30 km tangent altitude. The black curve indicates total radiance. The other curves indicate radiance for single emitter atmospheres (see legend). The noise level of the observations will be about $1\,\mathrm{nW}\,(\mathrm{cm}^2\,\mathrm{sr}\,\mathrm{cm}^{-1})$. The black arrow indicates the CO_2 Q-branch analysed in the retrievals.

tangent point locations
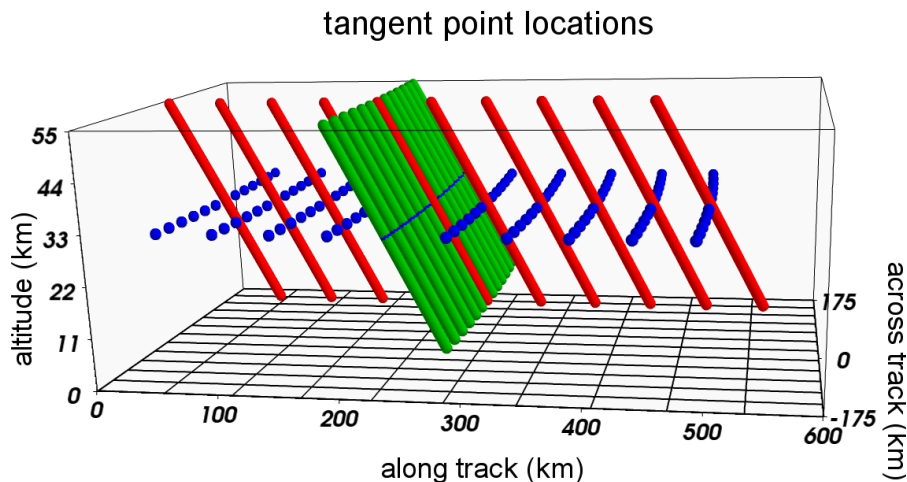
Fig. 2. Illustration of the PREMIER IRLS dynamics mode measurement grid. Symbols indicate the locations of tangent points of individual measurements. The green coloured spheres represent the measurements of a single image of PREMIER. Each blue orb represents a full profile and thereby the horizontal component of the measurement grid of ten consecutive images. In our simulations, we generally use only measurements of the central track, of which ten consecutive vertical measurement profiles are shown coloured in red. As the tangent points of a single profile are spaced at vertical intervals of 500 m, the orbs representing it are merged into a vertical line. The across track displacement of tangent points for the outermost measurement tracks is up to 2.2 km from the centreline.
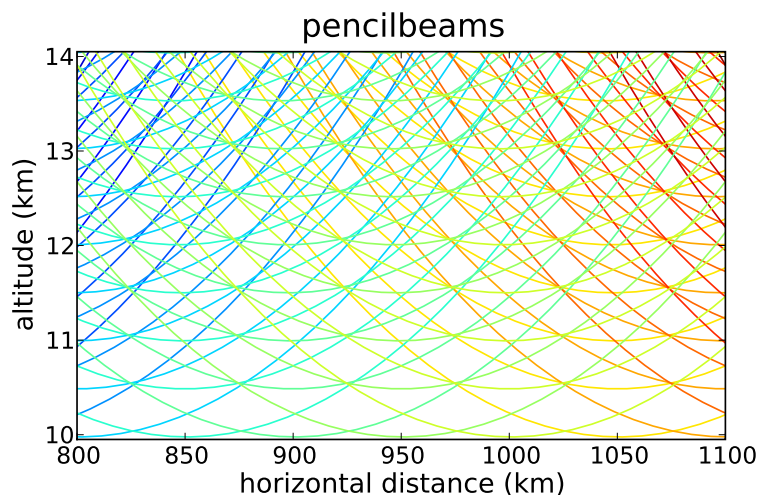
Fig. 3. Line-of-sights (LOS) of the central measurement track in the PREMIER IRLS dynamics mode. LOS belonging to the same image are assigned the same colour. Note that the plot shows only a minor subset of the full simulated atmospheric slice of 6000 km times 80 km.

Title Page

Abstract | Introduction

Conclusions | References

Tables | Figures

|◄ | ►|

◄ | ►

Back | Close

Full Screen / Esc

Printer-friendly Version

Interactive Discussion
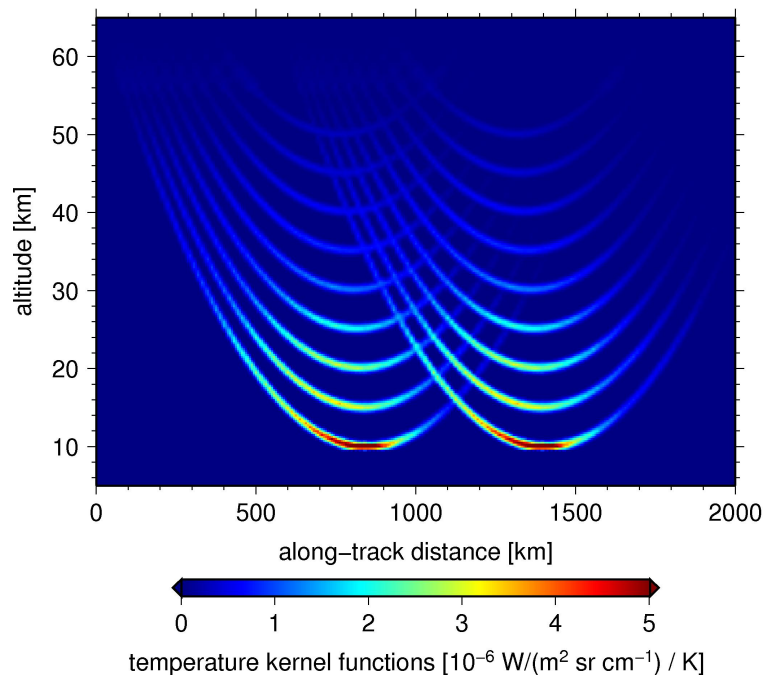
Fig. 4. Temperature kernel functions for the PREMIER IRLS at 790.75 cm^{-1} for mid-latitude atmospheric conditions. Kernel functions are superimposed by taking the maximum sensitivity at each atmospheric grid point. The plot shows kernel functions for 10, 15, . . . , 55 km tangent point altitude. Tangent points are separated by 500 km horizontal distance. Note that the measurement grid of the instrument is ten times finer in the vertical and horizontal domain than presented in this figure. The instrument is located on the left.
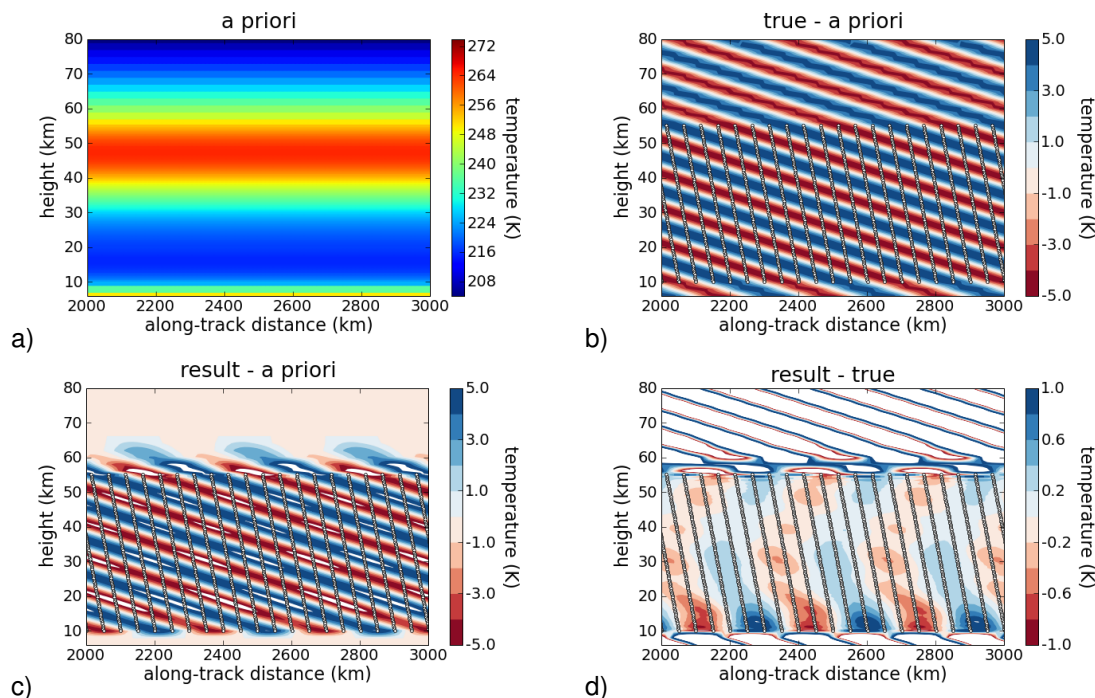
Fig. 5. Example of a retrieval end-to-end test used for generating the observational filter. A wave perturbation with 10 km vertical wavelength and 320 km horizontal wavelength is super-imposed onto the a priori atmosphere depicted in **(a)**. The difference between the disturbed atmosphere and the a priori is shown in **(b)**. The difference between the retrieval result and the a priori – that is the retrieved wave perturbation – is depicted in **(c)** and the difference between the result of the retrieval and the true state is depicted in **(d)**. The tangent points of the satellite measurements are shown as white circles. Please note that the horizontal retrieval grid is four times finer than the measurement grid. For better representation of the investigated structure only kilometres 2000 to 3000 of the simulated 6000 kilometres are shown.

Title Page

Abstract | Introduction

Conclusions | References

Tables | Figures

◄◄ | ►►

◄ | ►

Back | Close

Full Screen / Esc

Printer-friendly Version

Interactive Discussion
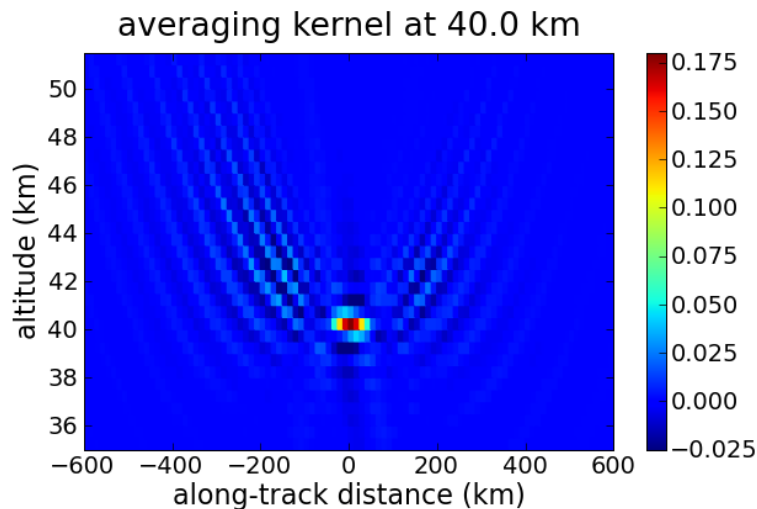
Fig. 6. Plot of the averaging kernel of a single atmospheric state vector element located in the middle of the atmosphere at 40 km height. Each coloured box represents the influence of the atmospheric grid point of the true atmosphere on a single sample of the retrieval result. Its shape is typical for averaging kernels of elements between 15 km and 50 km height.
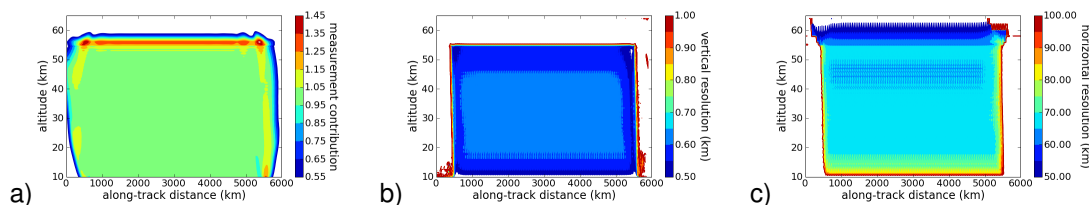
Fig. 7. Shown are the measurement contribution, vertical and horizontal resolution for a baseline retrieval with no modulated wave structure (i.e. the atmosphere of Fig. 5a). Tangent points of measurements lie between ≈10 km and 55 km vertically and ≈500 km and 5500 km horizontally.
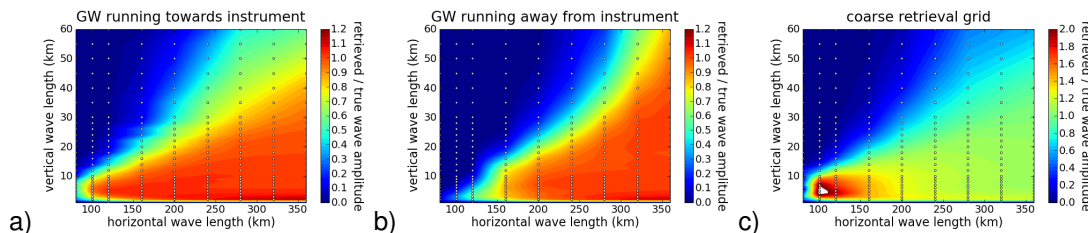
Fig. 8. Observational filter for the PREMIER IRLS. Depicted is the ratio of retrieved wave amplitude to true wave amplitude for the baseline retrieval setup with varying modulated waves. Analysed wavelength combinations are indicated with white circles. **(a)** shows the filter for the baseline setup with waves running towards the instrument. **(b)** shows the filter for a negative horizontal wave number (i.e. waves that run away from the instrument). **(c)** shows the observational filter derived with a sampling grid of 50 km horizontal distance instead of the usually employed 12.5 km. Please note the different colour scale compared to (a) and (b).
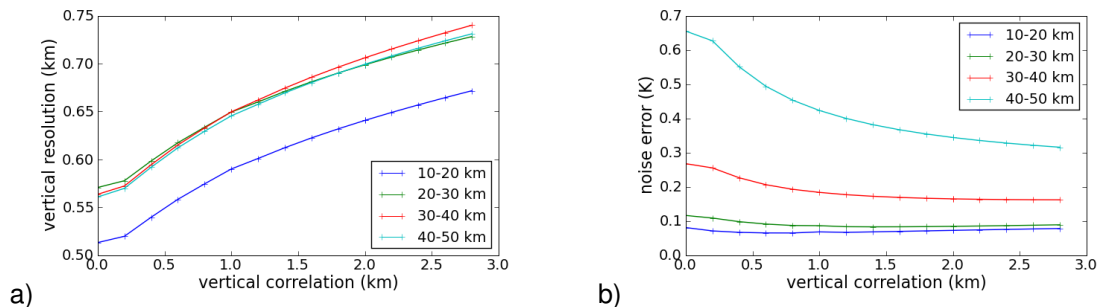
Fig. 9. The effect on vertical correlation length on vertical resolution and noise error. The average resolution and retrieval noise for the four major height ranges are depicted. One can clearly see the tradeoff between vertical resolution and retrieval noise.
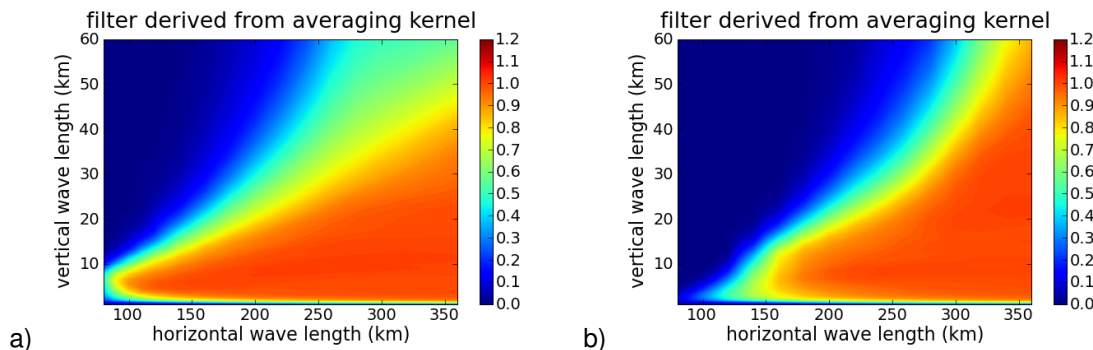
Fig. 10. The gravity wave filter as deduced from the averaging kernel. Each rectangle represents the mapping of a wave onto itself. **(a)** shows the diagonal elements for waves running towards the instrument (see also Fig. 8a), **(b)** shows the diagonal elements for waves running away from the instrument (see also Fig. 8b).

Tomographic retrieval approach for gravity wave observations

J. Ungermann et al.
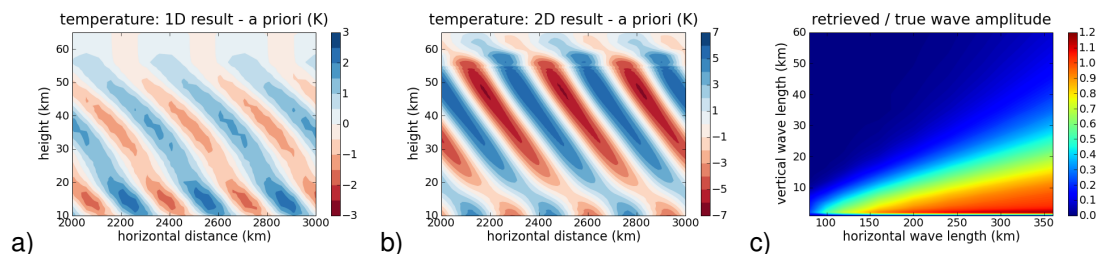
Fig. 11. This shows the retrieval result for **(a)** a series of conventional 1-D retrievals on the left and **(b)** a 2-D retrieval in the middle for a wave with 30 km vertical and 320 km horizontal wavelength. The climatological background profile was subtracted from the result. On the right, **(c)** depicts the gravity wave observational filter for a 1-D retrieval.

Title Page

Abstract | Introduction

Conclusions | References

Tables | Figures

◄◄ | ►►

◄ | ►

Back | Close

Full Screen / Esc
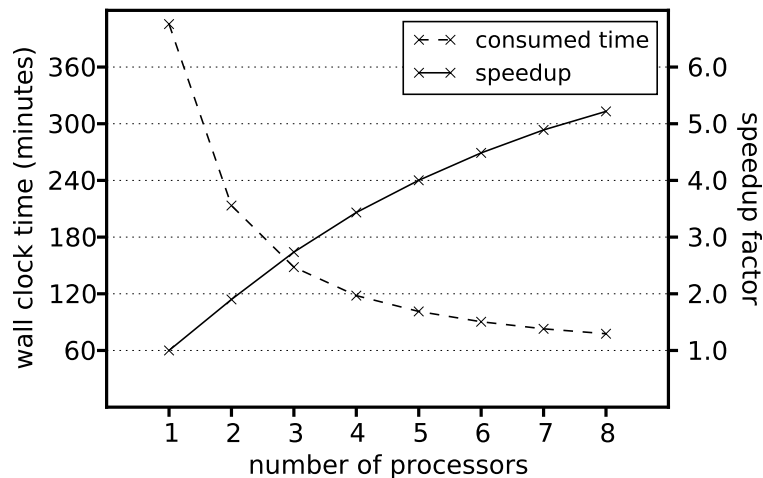
Printer-friendly Version

Interactive Discussion

Fig. 12. Consumed wall clock time and achieved speedup factor for the baseline retrieval if an OpenMP parallelisation is applied.